Materials Horizons

Critical role of pore size on perfluorooctanoic acid adsorption behaviors in carbonaceous sorbents

Journal:	*Materials Horizons*
Manuscript ID	MH-COM-12-2024-001771.R1
Article Type:	Communication
Date Submitted by the Author:	05-Feb-2025

Complete List of Authors:	Robertson, Mark; University of Southern Mississippi, School of Polymer Science and Engineering Lamb, Bradley; University of Southern Mississippi, Polymer Science and Engineering Griffin, Anthony; University of Southern Mississippi, School of Polymer Science and Engineering He, Lilin; ORNL, Ma, Boran; University of Southern Mississippi, Polymer Science and Engineering Qiang, Zhe; University of Southern Mississippi, School of Polymer Science and Engineering

New Concepts:

This work provides one of the first direct experimental observations of PFAS morphologies within confined pores in sorbents for the remediation of contaminated water sources. While previous studies have inferred potential PFAS aggregate morphologies based on adsorption behaviors and simulation results, these structures had not been quantitatively investigated through experimental methods. Using contrast-matching small-angle neutron scattering, this work reveals the size and shape of adsorbed PFAS morphologies in carbonaceous sorbents with varying pore sizes and sorbate concentration. Increased pore size facilitates multi-layer sorption behaviors within the pores, leading to enhanced performance. These observations are further supported through simulation results and physisorption experiments.

Data Availability Statement

The data supporting this article have been included as part of the Supplementary Information.

Critical role of pore size on perfluorooctanoic acid adsorption behaviors in carbonaceous sorbents

Mark Robertson,[1] Bradley Lamb,[1] Anthony Griffin,[1] Lilin He,[2,] Boran Ma,[1,*] Zhe Qiang[1,*]*

1. School of Polymer Science and Engineering, University of Southern Mississippi, Hattiesburg, Mississippi 39406, United States

2. Neutron Scattering Division, Oak Ridge National Laboratory, Oak Ridge, Tennessee 37831, United States

Corresponding Author

* Lilin He – Email: hel3@ornl.gov

* Boran Ma – Email: boran.ma@usm.edu

* Zhe Qiang – Email: zhe.qiang@usm.edu

ABSTRACT: Per- and polyfluoroalkyl substances (PFAS) are an emergent threat to the environment due to their toxic, carcinogenic, and environmentally persistent nature. Commonly, these harmful micropulltants are removed from contaminated water sources through adsorption by porous sorbents such as activated carbon. While studies suggest a relationship between sorbent pore size and their PFAS remediation performance, the underlying mechanisms—particularly

those related to sorbate morphology—have not been elucidated through direct experimental observations. This work investigates how pore size in carbonaceous sorbents impacts the morphology of adsorbed perfluorooctanoic acid (PFOA) aggregates and their sorption behavior, using microporous and mesoporous carbons as models. Contrast-matching small-angle neutron scattering (CM-SANS) determines the structure of adsorbed PFOA molecules, supported by molecular dynamics simulations and physisorption experiments. Our findings reveal that the larger pore sizes in mesoporous sorbents enable the formation of PFOA assemblies during adsorption, which is hindered in microporous sorbents. Collectively, this work provides direct insights into the adsorption and assembly mechanisms of PFAS molecules within confined pores, offering important insights for the rational design of effective remediation systems.

Introduction

Per- and polyfluoroalkyl substances (PFAS) are a class of emergent chemical contaminants that have spread to hundreds of sites around the world and are present in up to 97% of American's bloodstreams.[1–3] These contaminants have been reported to increase cancer risks in addition to causing negative reproductive and metabolic effects.[4–7] PFAS are used in various industries including many consumer products, foams for firefighting, and the production of fluoropolymers, resulting in their widespread and uncontrolled contamination into soil and water sources.[8,9] The increased presence of PFAS in ecosystems has spurred aggressive legislative action, including banning the use of many legacy PFAS, as well as establishing stringent environmental standards. Specifically, in 2022, the United States Environmental Protection Agency (EPA) established a

health advisory level for the most common PFAS, perfluorooctanoic acid (PFOA), of 0.004 ppt (parts per trillion).[10] The recognized hazards of these materials, even at extremely low concentrations, and their known adverse health impacts, highlight the urgent need for their effective remediation.

While PFAS represent a class of 1000s of synthetic compounds with diverse chemical identities, they generally consist of a surfactant-type structure, including a fluorinated hydrophobic tail and a hydrophilic headgroup such as a carboxylic acid, sulfonic acid, or sulfonamide.[11,12] The presence of strong C-F bonds, and associated weak intermolecular forces, gives rise to many unique properties in PFAS including excellent chemical and thermal stability, and strong hydrophobic interactions among many other interesting characteristics. While there are many methods for removing PFAS from contaminated sources, adsorption based technologies continue to be the most promising for multiple reasons, including their low production costs, ability to be deployed at scale, and low energy requirements during operation compared to other potential technologies such as bioremediation,[13,14] oxidation,[15–18] and photocatalytic reduction methods.[19–21] Additionally, adsorption technologies are widely used in numerous wastewater treatment plants and the existing infrastructure can support the integration of new materials for PFAS remediation.[22]

Currently, despite many exciting new developments in sorbent technologies, such as covalent organic frameworks (COFs),[23–26] metal organic frameworks (MOFs),[27–30] fluoropolymers,[31–33] and cyclodextrins,[34–36] show great potential for PFAS sorption, the most widely employed materials for PFAS adsorption are commercially available activated carbons

(AC).[37–41] Briefly, AC are porous carbon materials containing large amounts of micropores (pore size < 2 nm) which provide high specific surface areas (typically larger than 500 m^2/g) for the sorption of guest molecules. AC is historically established for the removal of common micropollutants from wastewater streams,[42,43] which has also been thoroughly investigated for the adsorption of PFAS molecules.[38,44,45] However, their adsorption efficiencies for PFAS are often found to be unsatisfactory, including slow sorption kinetics and low sorption capacity due to multiple reasons. Firstly, these AC-PFAS interactions are primarily through hydrophobic-hydrophobic interactions between the carbon material and fluorinated carbon tail of the PFAS molecule, as suggested in previous works.[46,47] Secondly, limited pore connectivity in AC hinds the transport of PFAS through its disordered structures.[48,49] A notable study by Zappi et al. investigated the impact of pore size in carbon-based materials on their PFOA remediation from water, specifically comparing AC with ordered mesoporous carbon (OMC) sorbents, which contain pore sizes of approximately 5 nm in diameter with long-range order.[50] The PFOA adsorption capacity of OMCs was found to be 2-5 times higher than that of AC sorbents, while also reaching equilibrium significantly faster. Furthermore, the adsorption isotherm results for the OMC system suggested a Freundlich-like adsorption mechanism, which appears to be correlated with the formation of layered structures within the sorbents rather than monolayers. While these studies highlight the potential for forming complex morphologies of adsorbed PFAS aggregates by varying the pore size of carbon sorbents, which is a critical factor in determining the adsorption efficiency of porous materials, a fundamental investigation into these hypotheses remains underexplored. This knowledge gap limits the development of rational design principles for

sorbent design tailored for PFAS remediation, hindering progress in achieving more efficient and scalable solutions.

This work investigates the instrumental role that pore size can play in controlling the morphology of adsorbed PFAS aggregates within carbonaceous sorbents, which directly influence their sorption performance. A commercially available AC sorbent and a conventional soft-templated OMC sorbent with averaged pore diameter of 8.0 nm are employed as model systems. The morphology of adsorbed PFOA aggregates as a function of solution concentration is revealed through contrast-matching small angle neutron scattering (CM-SANS) studies, which suppresses the scattering contributions of the porous nanostructure and enable the quantitative determination of the size and shape of adsorbed PFOA. The scattering results are further elucidated through atomistic molecular dynamics (MD) simulations which illustrate the morphological evolution of PFOA through the adsorption process. Additionally, these results are supported through physisorption experiments that indicate changes in pore texture after adsorption of the PFOA molecules and highlight the role of mesoporosity in the adsorption process. This work provides critical experimental insights into the role of pore size in dictating PFAS assembly formation during adsorption, laying a foundational understanding to guide the rational design of advanced porous sorbents for enhanced PFAS remediation.

Experimental

Materials

Powder activated carbon (AC) was received from Calgon Carbon, and soft-templated ordered mesoporous carbon (OMC) sorbents were synthesized following procedures established in the literature.[51] Pluronic F127 was purchased from Sigma-Aldrich and a phenolic resin (resol) was synthesized following a previous report.[52] Perfluorooctanoic acid (PFOA) was purchased from TCI chemicals, and deuterated water (D_2O) was purchased from Sigma Aldrich. DI water was obtained using a Millipore Sigma Mill-Q IQ 7003 ultrapure purification system.

Adsorption Experiments

Adsorption experiments were conducted by dissolving PFOA in DI water at a range of concentrations from 1 mg/L to 100 mg/L. Each of the sorbents were included into the solutions at a sorbent dosage of 5 mg/mL. The samples were equilibrated over 24 h while shaking at 100 rpm on an orbital shaker, removed through filtration, and dried at 40 ˚C under vacuum to remove residual moisture. After drying, the sorbents were used for further experiments.

Characterization

Nitrogen physisorption isotherms were generated using a Tristar II 3020 from Micromeritics at 77 K. The Brunaeur Emmett Teller (BET) approach was employed to determine the specific surface areas of the sorbents, and the pore size distributions were calculated from the adsorption branches of the isotherms through nonlocal density functional theory (NLDFT). Changes in pore texture were determined by comparing nitrogen physisorption isotherms before and after adsorption of PFOA from solutions of varying concentration. Specifically, the decrease in BET surface area, total pore volume, or mesopore volume was determined using the following equation:

$$Percent\ Decrease = \frac{X_i - X_f}{X_i} \times 100\% (1)$$

where X_i is the value of interest for the sorbent prior to adsorption and X_f is the value of interest for the sorbent after adsorption. Scanning electron microscopy (SEM) experiments were conducted using a Zeiss Ultra 60 field emission SEM at an accelerating voltage of 20 kV. X-ray photoelectron spectroscopy (XPS) survey scans were recorded using an ESCALAB Xi+ spectrometer from Thermo Fisher which employed a monochromatic Al Kα X-ray source and charge compensation at a takeoff angle of 90° and a base pressure of 3 x 10^{-7} mbar. All survey scans were analyzed through Avantage software from Thermo Fisher.

Small Angle Neutron Scattering Experiments

As SANS might not be often employed in environmental science, a brief introduction to SANS fundamentals, in addition to more in depth discussions regarding experimental procedures are provided in the Supplmentary Information. Additionally, the reader can refer to multiple excellent reviews that cover SANS for polymer and soft matter systems and SANS fundamentals in great detail.[53,54] For the sake of clarity for a broad audience, an introduction to the physical mechanisms which are basis of neutron scattering techniques, in addition to more detailed discussions regarding the model selection and fitting procedures are found in the Supporting Information. All SANS experiments were performed using the general-purpose SANS (GP-SANS) instrument at the High Flux Isotope Reactor (HFIR) within Oak Ridge National Laboratory (ORNL).[55] Demountable sample cells were loaded with the dried sorbent samples then filled with D_2O for contrast matching. The neutron wavelength was 4.72 Å with a wavelength spread $\Delta\lambda/\lambda$ of 0.13. The background

scattering from the instrument and sample holders was removed during data reduction, and corrections were applied for detector efficiency, sample thickness, and transmission. Additionally, the scattering intensity was placed on an absolute scale using a pre-calibrated standard. The scattering results for a q-range from 0.015 nm^{-1} to 8.1 nm^{-1} were fitted to a generalized scattering function, Equation 2:

$$I(q) = \mathrm{A}F(q)\,S(q) + Bq^{n} + \mathrm{C} \quad (2)$$

Where A is a scaling factor, I(q) is the scattering intensity, F(q) is the form factor, and S(q) is the structure factor as a function of the scattering vector, q. C represents background scattering. The term Bq^n represents power law scattering from the particle surface, which is dominant in the low-q regime between 0.015 nm^{-1} and 0.4 nm^{-1}. At this relatively low-q range, the power law scattering can be attributed to interfacial scattering of large scale structures, such as the surface of the carbon sorbent particles. In both the AC and OMC sorbents, a cylindrical form factor is employed to describe the size and shape of the adsorbed PFOA aggregates,[56] which is described by Equation 3:

$$F(q) = 2\Delta\rho V \frac{sin\left(\frac{1}{2}qLcos(\alpha)\right)}{\frac{1}{2}qLcos(\alpha)} \frac{J_1(qRsin(\alpha))}{qRsin(\alpha)} \quad (3)$$

where R and L are the radius and length of the adsorbed cylindrical PFOA aggregate, J_1 is the Bessel function of the first kind, α is the orientation of the cylinder with respect to q, and $\Delta\rho$ is the scattering length density (SLD) contrast between the PFOA molecule and the surrounding D_2O. The difference in SLD between the PFOA and carbon/D_2O regions within the sample dictates the intensity of coherently scattering neutrons after interaction with the incident neutron beam. During

the fitting procedure, the SLD contrast was held constant using calculated values for PFOA and D_2O while the length and radius of the cylinder were varied to minimize the error of the fitting result. Given the absence of a mechanism to orient the aggregates in any direction, these results are averaged over all possible orientations. A cylinder form factor is employed to model the adsorbed PFOA aggregates due to the characteristics of the molecule itself. The large fluorine atoms of the PFOA molecule result in significant steric repulsion, making them relatively rigid molecules, and therefore we believe it is suitable to approximate the dimensions of the molecule to be cylindrical in nature. While aggregates of multiple molecules may not be perfectly cylindrical in nature, using a cylinder form factor reduces the number of assumptions and parameters required to fit the scattering results, while remaining a reasonable approximation of the aggregate structure. It is noted that other works investigating similar systems employ a core-shell cylinder form factor which models the adsorbed aggregates as uniform coatings that can grow in thickness towards the center of the pore and in length along the pore. In those works, the investigated concentrations are typically much larger than this study.[57,58] To simplify the model fitting and reduce the number of assumptions made, a cylinder form factor is employed to describe the adsorbed PFOA molecules. Additionally, the disordered nature of the pore structures within AC results in scattering that does not require the use of a structure factor due to the lack of pore-to-pore correlations; The use of a structure factor is only applicable in the OMC sorbents which has an ordered, hexagonally-packed cylindrical nanostructure. In the case of a perfect 2-dimensional lattice with a hexagonally-nanostructure, the structure factor could be represented by a series of delta functions corresponding to the Miller indices of the unit cell due to Bragg reflections by the ordered nanostructure.

Imperfections in the nanostructure of the OMC sorbent used in this work, in addition to the relatively limited resolution of SANS instrumentation result in significant broadening of these peaks. Therefore, the structure factor in the OMC sorbent is determined as the sum of 3 gaussian peaks associated with Bragg reflections by the lattice of the hexagonal nanostructure, which has been previously employed in the literature.[59] The position and breadth of these peaks are varied during the fitting procedure in addition to the length and radius of the cylindrical form factor. The position and breadth of these Gaussian functions are related to the distance between planes of scatterers and the strength of the spatial correlation between those planes, respectively. In the low-q regime from 0.015 nm^{-1} and 0.4 nm^{-1}, power-law scattering from interfaces of the carbon sorbent particles dominates the scattering pattern. In the OMC samples, this becomes convoluted with the form factor and structure factor until the power law scattering is insignificant at scattering vectors $q > 0.4$ nm^{-1}. Since very limited information relevant to this study can be gained from the power-law scattering, has been excluded in the OMC samples to reduce complexity during model fitting.

Molecular Dynamics Simulations

The atomistic MD simulation contained water, represented by the SPC/E model,[60] as well as PFOA and sodium ions for charge balancing, both described by the GROMOS 54A7 force field, which have shown good agreement with experimental results.[61] A graphene sheet, modeled via an uncharged Lennard-Jones potential, was used to represent the sorbent surface. The optimized topology for PFOA was generated using the Automated Topology Builder (ATB),[62] which utilizes density functional theory to obtain an optimized structure through quantum mechanical

calculations. Additionally, the dimensions of the PFOA molecule were able to be calculated from the distance between the tail fluorine and the head oxygen from the optimized geometry. A simulation cell, featuring periodic boundaries in the x and y directions and fixed boundaries in the z direction, with dimensions of 58.9 Å × 63.8 Å × 90 Å was constructed around the graphene sheet to accommodate bonds across the periodic boundary. The MD simulations were carried out in the NVT ensemble using the Large-scale Atomic/Molecular Massively Parallel Simulator (LAMMPS).[63]

Initially, the simulation contained only water and the graphene sheet. PFOA molecules were then incrementally added at 1 ns interval, up to a total concentration of 20 vol%. A biased approach (details provided in the Supplementary Information) was utilized to accelerate adsorption dynamics, improving computational efficiency. To maintain a solution density of 1 g/cm³, water molecules were removed with each PFOA addition. The simulation trajectory was subsequently analyzed with in-house Python scripts, utilizing the MDAnalysis package,[64] and results were visualized using OVITO.[65] Morphological evolution was monitored over the course of the simulation, and pair correlations averaged over 2.5 ns, after the addition of all PFOA, using MDAnalysis to characterize the adsorbed structures.

Results and Discussion

This work employs PFOA as the target sorbate, which is the most common and legacy PFAS molecule found in contaminated water sources and consists of a fluorinated carbon tail and a carboxylic acid head group, as depicted in Figure 1(A). The dimensions of the PFOA molecule

can be estimated as a rod-like structure and calculated from the optimized PFOA molecular model obtained from the ATB database, accounting for atom sizes, bond angles and bond lengths.[62] Through this method, the PFOA molecule is estimated to have a length of 1.13 nm and a diameter of 0.338 nm. Nitrogen physisorption isotherms (Figure 1(B)) were employed to determine the pore characteristics and calculate the pore size distributions of both AC and OMC sorbents (Figure 1(C)). Specifically, AC exhibited a specific surface area of 710 m^2/g and a pore volume of 0.85 cm^3/g while the OMC sorbent had a specific surface area of 685 m^2/g and pore volume 0.88 cm^3/g. The isotherm of the AC sorbent exhibits a large increase in quantity adsorbed at low relative pressures which indicates the presence of micropores. Similarly, the isotherm for the OMC sorbent indicates an increase at low relative pressures, suggesting the presence of microporosity, but also contains type IV hysteresis at intermediate relative pressure and confirms the presence of mesopores. The pore size distributions derived from the adsorption branch of the isotherm confirm that the AC sorbent is predominantly microporous. In contrast, the OMC sorbent exhibits a uniform pore size distribution centered around 8 nm, along with a significant fraction of micropores. These distinct porous carbons were employed as model systems to investigate the impact of pore size on the adsorption of PFOA. The sorbents were further characterized through both scanning electron microscopy (SEM) and x-ray photoelectron spectroscopy (XPS). Through SEM images provided in Figure S1, it is demonstrated that the macroscopic sorbent particles are similar in shape and size which ranges from ~200 μm – 1000 μm. XPS survey scans (Figure S2 and Table S3) indicate very similar chemical compositions where the AC sorbent contains 90.6 at% carbon and 8.0 at% oxygen, with roughly 1.4 at% of trace impurities which are all less than 1

at%, respectively. Similarly, the OMC sorbent exhibits a composition of 89.7 at% carbon, 7.8 at% oxygen, 1.0 at% sodium (byproducts from sample preparations), and 1.5 at% or trace impurities. The similarity in macroscopic particle size and shape, and the general chemical composition further isolates the impact of pore size on the adsorption of the PFAS molecules.

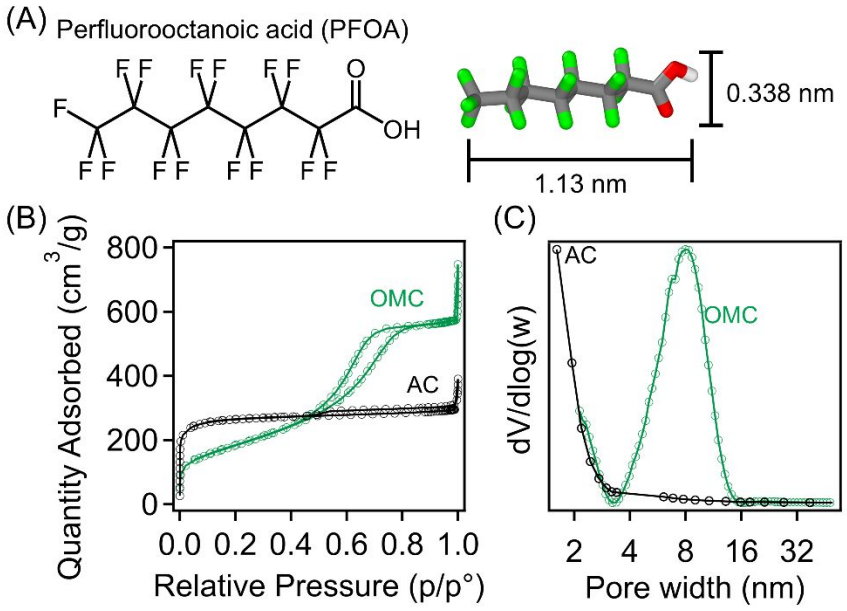

Figure 1. (A) Chemical structure and calculated dimensions of the PFAS molecule used in this study as a model system, perfluorooctanoic acid (PFOA). (B) Nitrogen physisorption isotherms of commercially available activated carbon (AC) and ordered mesoporous carbon (OMC). (C) Pore size distributions of the AC and OMC sorbents indicating the presence of micropores and mesopores, respectively.

SANS measurements under contrast matched conditions were employed to investigate the morphologies of adsorbed PFAS aggregates within the pores of the carbonaceous sorbents. Figure 2(A) schematically illustrates the effect of contrast matching during SANS experiments.

Specifically, backfilling the pores of the sorbents with a solvent having a similar scattering length density (SLD) (D_2O; SLD = 6.37 x 10^{-6} $Å^{-2}$) to that of the carbonaceous matrix (SLD = 6.33 x 10^{-6} $Å^{-2}$) masks the scattering contributions that result from the contrast between the void of the pores and the matrix of the sorbent. When the pores are filled with molecules which have a distinct SLD from their surroundings, like PFOA (SLD = 3.80 x 10^{-6} $Å^{-2}$), the scattering results from the contrast between the molecules and their surrounding environment. Therefore, this method can be used to extract information about the size and shape of adsorbed PFOA aggregates within the carbonaceous sorbent without requiring deconvolution of scattering contribution from the porous nanostructure.

Prior to loading with PFOA and contrast matching, the disordered microporous structure of the AC sorbent results in a broad scattering feature (Figure 2(B)) while the scattering pattern of the OMC sorbent contains distinct primary and secondary scattering peaks which are related to the Bragg reflections of the ordered nanostructure (Figure 2(C)) due to the highly ordered porous nanostructure common for OMC materials. The primary scattering peak corresponds to (100) reflection and the secondary peak is due to the convolution of the higher-order reflection (110) and (200) reflections. These scattering features from the pore structures within the sorbents are completely removed from the scattering patterns after saturating the pores with D_2O, indicating successful contrast matching. When contrast matching is applied to sorbents loaded with PFOA molecules, distinct features emerge in the scattering patterns, reflecting the associated PFOA structures. In the OMC sorbent system, this phenomenon reveals that the adsorbed molecules conform to the shape of the pores within the carbon matrix, suggesting effective PFOA sorption

in mesopores with long-range structural correlation. These scattering patterns can then be modeled using aforementioned fitting functions to extract quantitative data on the size and shape of the adsorbed aggregates.

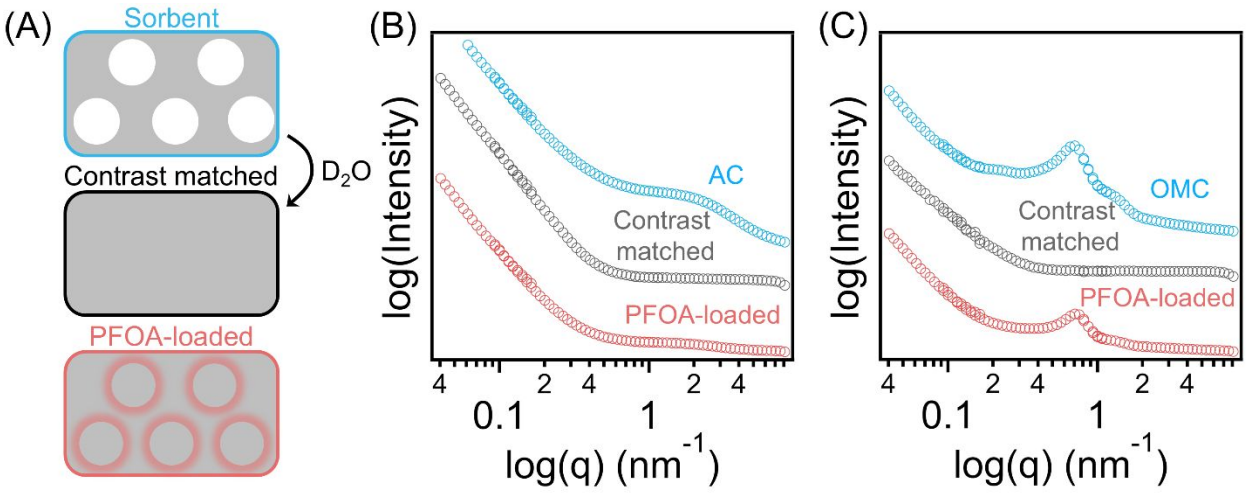

Figure 2. (A) Schematic illustration of the effects of contrast matching during SANS experiments on PFOA-loaded porous carbon. Scattering patterns of the (B) AC and (C) OMC neat sorbents, under contrast matched conditions, and under contrast matched conditions after loading with PFOA molecules.

To investigate the assembly mechanism of PFOA in both AC and OMC sorbents, adsorption experiments were carried out in PFOA solutions ranging in concentration from 1mg/L to 100 mg/L. It is worth noting that these concentrations are multiple orders of magnitude lower than the critical micelle concentration of PFOA (~11000 mg/L),[66,67] thus preventing self-assembly into micellar structures prior to adsorption by the sorbent. Additionally, while PFAS concentrations in practical applications are typically much more dilute, studying sorption mechanisms and processes

at mg/L concentrations remains important to mimic the high local concentrations that form on the sorbent surface. The samples were allowed to equilibrate over 24 h and were subsequently dried at 40 ˚C under vacuum. After drying, the samples were loaded into cells for scattering experiments with D_2O for contrast matching. The scattering results are depicted in Figure 3. Despite the 100-fold increase in PFOA concentration during adsorption experiments, the scattering patterns of the AC sorbent system are very similar. The scattering intensity shows only a slight increase with higher PFOA concentrations, indicating inefficient PFOA adsorption. In a sharp contrast, the scattering results for the OMC sorbents exhibit significantly increased scattering intensity with increasing PFOA concentration during the adsorption process in addition to the primary scattering peak becoming increasingly distinct. This suggests that PFOA molecules can conform to the shape of the ordered nanostructure during the adsorption process. The scattering patterns, model fits as described in the experimental section (eq 2), and compiled results from the cylinder form factor (eq 3), are found in Figure 3. Additional parameters used during the model fitting procedure are found in Table S1 and S2. A cylinder form factor effectively fits the scattering data for the AC sorbent after PFOA adsorption under contrast-matched conditions (Figure 3(A)). Although the pores within AC are disordered and not cylindrical, the scattering contributions under contrast-matched condition are solely from scattering by the PFOA molecules. The steric repulsion between large fluorine atoms in the perfluorinated tail make the molecules significantly more rigid than their hydrocarbon counterparts,[68] therefore it becomes reasonable to estimate the individual molecules, and their aggregates, as cylindrical structures. Overall, the scattering patterns of AC show only a moderate change with increasing PFOA concentration during adsorption, yielding

similar cylinder radii and aggregate lengths regardless of the solution concentration. The results are presented as the open markers in Figure 3(C). Specifically, the cylinder radius increases from 0.15 nm at a concentration of 1 mg/L to 0.42 nm at 100 mg/L, while the aggregate length also only slightly increases from 1.9 nm to 2.46 nm. At the low concentration of 1 mg/L, the result aligns well with the size of a single PFOA molecule. We note the primary mechanism for PFAS adsorption onto carbonaceous sorbents is hydrophobic-hydrophobic interactions. Scattering results from a 100 mg/L PFOA concentration solution suggest structures consistent with aggregates formed by approximately 2 to 3 molecules stacked side-by-side due to favorable interactions between the fluorinated carbon tails. These aggregates are collectively adsorbed onto the surface of the AC pores. Although it has been previously postulated that the adsorption of PFOA can occur through the adsorption of micelles or hemi-micelles to AC,[69] these results indicate that the adsorption of PFOA onto micropores within AC does not facilitate the cooperative assembly of larger aggregates. Instead, it primarily leads to the formation of smaller aggregates consisting of only a few molecules, which are comparable in size to the critical micropore dimensions.

Figure 3(B) presents the scattering patterns under contrast-matched conditions for the OMC sorbent after PFOA adsorption. The inclusion of the structure factor in the fitting routine accounts for the contributions from aggregate-aggregate correlations and enables the extraction of information from the cylinder form factor that was also employed to model the aggregates in the AC system. While some previous works employed core-shell cylinder form factors to model the adsorption of surfactants within cylindrical mesopores,[57,58] a simple cylinder form factor is used in this work to reduce the number of assumptions regarding the adsorption mechanism employed

during the model fitting procedure. With increasing concentration during adsorption of PFOA, both the cylinder radius and aggregate length increase significantly. After adsorption from a 1 mg/L PFOA solution, it can be found that the cylinder radius is 0.49 nm with an aggregate length of 2.92 nm. These results are consistent with the formation of a multilayer PFOA structure adsorbed through hydrophobic interactions between the fluorinated tails and the carbonaceous pore wall that extends for multiple molecules along the length of the pore. Both the radius and length of the aggregates increase with increasing concentration during adsorption, reaching maximum values at 100 mg/L of 2.86 nm and 46.0 nm for the cylinder radius and aggregate length, respectively. These results indicate that a complex structure of PFOA can form during the adsorption process which can be explained by the molecules first adsorbing to the pore wall via their hydrophobic tails and subsequently growing towards the center of the pore and along the pore as additional molecules are attach to the aggregate. In contrast to the micropores within the AC samples, the larger mesopores (~8.0 nm) within the OMC samples accommodate larger PFOA aggregates and enables their assembly into larger nanostructures.

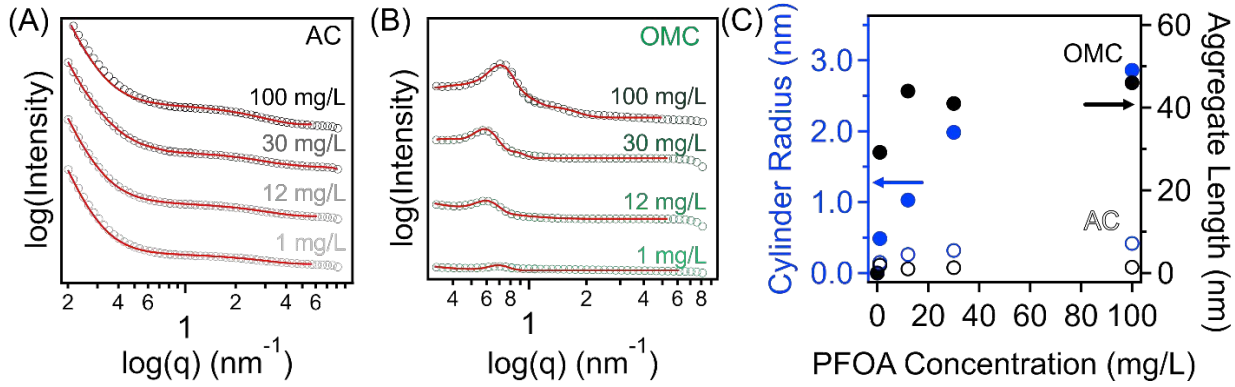

Figure 3. CM-SANS patterns of (A) AC and (B) OMC sorbents loaded with PFOA molecules from solution concentrations of 1 mg/L, 12 mg/L, 30 mg/L and 100 mg/L. The open markers are raw

scattering data after reduction of the 2-dimensional scattering patterns and the solid lines are fits to the scattering functions as described in the main text. The scattering patterns here are shifted vertically for clarity. (C) Cylinder radius and aggregate length results extracted from the form factors of both AC and OMC sorbents where AC results are represented by open markers and OMC results are depicted as closed markers.

The assembly of molecules within mesoporous materials during adsorption has been previously studied through SANS for numerous sorbates including proteins/polymers,[70,71] ionic liquids,[72] and other surfactants.[57–59] Generally, SANS results describing the adsorption of nonionic surfactants within mesoporous silica follow similar trends to those observed in the PFOA/mesoporous carbon model system investigated in this work. Specifically, the intensities of Bragg reflections increase with increased concentration of the surfactant during adsorption as more molecules fill the nanopores. This also coincides with an increase in adsorbed aggregate dimensions. For instance, Findenegg et al. investigated the adsorption behaviors of poly(ethylene oxide) surfactants onto mesoporous silica (SBA-15) with pore sizes of 8.1 nm through CM-SANS.[59] Through these experiments, it was determined that the adsorbed layer thickness, analogous to half of the cylinder radius in this work, of the adsorbed aggregates increased with increasing concentration of surfactants within the pores of the silica sorbent until reaching a maximum between 2.0 nm and 2.5 nm. Further increasing the surfactant concentration increases the adsorbed aggregate volume while the adsorbed layer thickness remains essentially constant and forms a patchy bilayer along the pore wall. This is a result of the adsorption mechanism of the surfactant with the hydrophilic pore walls of the silica sorbent. The hydrophilic hydroxyl head of the ethoxylated surfactant

preferentially adsorbs to the pore wall, enabling the formation of micellar structures, in contrast to the adsorption of PFOA in mesoporous carbon explored in this work. The adsorption of PFOA through the interactions between the hydrophobic tail prevents the formation of micelles, and ultimately enables the formation of aggregates with radii that are seemingly only restricted by the size of the pore. The difference in adsorption mechanism is a key driving force in altering aggregate formation in comparison to previous studies.

These results were further validated through molecular dynamics (MD) simulations of the adsorption of PFOA onto a graphene surface to mimic the interactions between the PFOA molecule and the carbonaceous surface of the OMC sorbents. Specifically, an all-carbon graphene sheet is employed as the bottom boundary of a 58.9 Å × 63.8 Å × 90 Å simulation box and PFOA molecules are introduced one molecule at a time and allowed to equilibrate, while also removing the appropriate number of water molecules to maintain a constant density. Snapshots of the simulation box after the addition and equilibration of 5 vol%, 10 vol%, 15 vol%, and 20 vol% of PFOA molecules are found in Figure 4 (A). It is worth noting that these concentrations do not reflect the concentration of the PFOA solution during the adsorption experiment, but rather illustrate the effect of increasing local concentration within the pores of carbon sorbents as more molecules diffuse into the material and are adsorbed. At 5 vol%, the PFOA molecules adsorb into a single layer along the graphene surface due to the favorable interactions between the hydrophobic fluorinated tail and the carbon surface. Additionally, the concentration at 5 vol% is roughly twice that of the critical micelle concentration, but no micelles are formed due to the more favored interactions between the molecules and the carbon surface. With increased volume percentage (10

vol%), molecules form a layered structure of 2 to 3 molecules that extends 1.0 nm from the surface of the graphene layer. As the PFOA concentration is increased within the simulation box, the layered structures transition to hemi-cylinder type structures where the PFOA molecules are anchored to the aggregates by the fluorinated surfactant tail, but the hydrophilic carboxylic acid head extends away from the graphene sheet (detailed views in Figure S3(A-B)). The thickness increases from 0.3 nm that corresponds to a single adsorbed layer along the carbon surface to approximately 2.4 nm for a more complex hemi-cylindrical structure, shown in Figure 4(A). This is in good agreement with the cylinder radius results characterized by SANS (Figure 3(C)). The MD simulations are further analyzed through pair correlation functions of the individual atoms in the molecules adsorbed directly to the graphene surface in Figure 4(B). The carbon-carbon correlation function suggests that the adsorbed layer is a uniform structure of PFOA molecules that are parallel to each other which is indicated by peaks at 6 Å, 12 Å, and 18 Å. These peaks correspond to molecules directly adjacent to each other and molecules separated by one and two PFOA molecules, respectively, as indicated by the insets in Figure 4(B). The oxygen-oxygen correlation function further illustrates that the molecules are adsorbed parallel to one another along the surface with some of the molecules oriented in a head-to-head fashion and others in a tail-to-tail fashion with respect to each other, indicated by peaks at 24 Å and 31 Å. Pair correlation functions for the remainder of the adsorbed aggregate are presented in Figure S3.

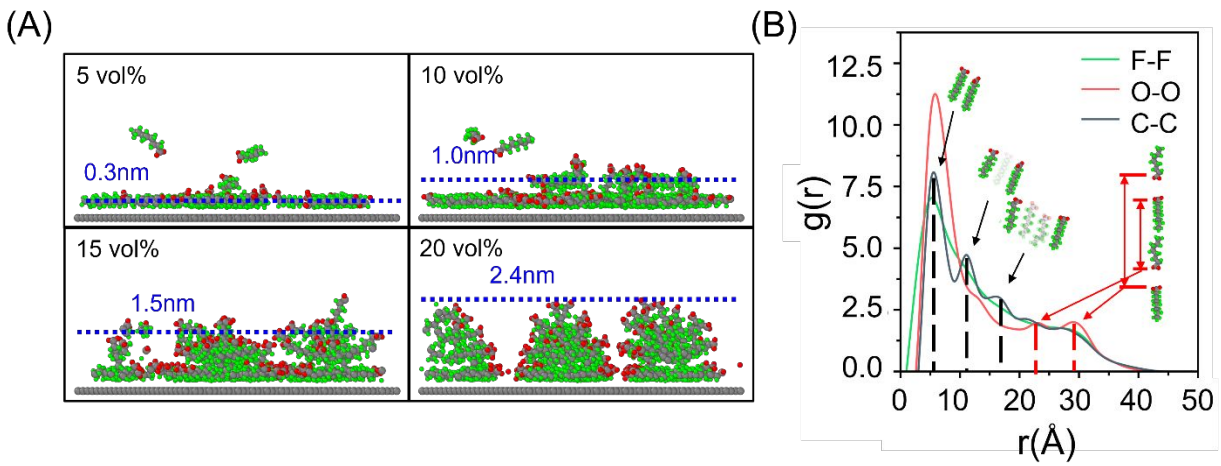

Figure 4. (A) Molecular dynamics simulation results of PFOA adsorbed to graphene with gradually increased concentration (5 vol%, 10 vol%, 15 vol%, and 20 vol%) of PFOA within the simulation box to mimic the increased concentration of molecules within the pores of the sorbent as they diffuse into the carbon matrix. Adsorbed PFOA aggregates show increase in thickness as concentration increases, from 0.3 nm to 2.4 nm, at 5 vol% and 20 vol%, respectively. (B) Pair correlation functions of carbon-carbon, oxygen-oxygen, and fluorine-fluorine pairs at the highest concentration of PFOA within the simulation box after equilibration.

To further understand the impact of PFOA morphology and assembly mechanisms on its sorption capacity in different porous sorbents, nitrogen physisorption experiments were conducted on ACs and OMCs after PFOA adsorption at varying solute concentrations; this analysis aims to assess how the pore textures of the sorbents influence sorption performance. The physisorption isotherms can be found in Figure S4, while the compiled results for AC and OMC are found in Figure 5(A) and Figure 5(B), respectively. For the AC sorbent, minimal decreases in BET surface area (BET), total pore volume (PV), and mesopore volume (MePV) after adsorption of PFOA from

solutions of 1 mg/L and 12 mg/L. After adsorption from a 30 mg/L solution, the BET surface area, PV, and MePV decreased by 22%, 21%, and 17%, respectively. These values remain relatively similar after adsorption from a 100 mg/L (BET = 16%; PV = 20%; MePV = 22%). The relatively limited changes in pore texture with increasing solution concentration, when compared to neat AC samples, further reinforce the conclusions drawn from the SANS results. Specifically, at low concentrations, the characteristics exhibit minimal changes as molecules have not occupied the pore structures within the sorbent. At increased concentrations, the decreases in BET surface area, pore volume, and mesopore volume indicate more pores are being occupied by the PFOA molecules. However, a large portion of these pores remain unoccupied by the PFOA molecules, suggesting the small pore sizes are restricting the effective use of the pore structures within the sorbent, although they are still accessible to N_2 molecules to perform physisorption measurements. This further indicates that the primary adsorption of PFOA occurs on the particle surface of AC sorbents, rather than within the micropores. This has been demonstrated by a recent work which found that adsorption to particle surfaces drives the adsorption of PFAS molecules at short times, and the quantity adsorbed only increases slightly due to intraparticle diffusion of the molecules into micropores.[73] As shown in Figure 5(B), the changes in pore texture after adsorption of PFOA are much more significant for the larger pore, OMC sorbent. After adsorption from the 1 mg/L solution, the BET surface area decreases by 24%, suggesting significant adsorption of the PFOA molecules. Furthermore, the mesopore volume decreases by 77% while the total pore volume decreases by only 31%. This result suggests that the mesopores in the sorbent are primarily contributing to the adsorption of PFOA, which allows the formation of multilayer structures of

PFOA molecules within the pore surface. These pore characteristics further decrease with increasing solution concentration, resulting in a 96%, 97%, and 97% decrease in BET surface area, total pore volume, and mesopore volume, respectively, after adsorption from a 100 mg/L PFOA solution. Altogether, comparing the changes in pore characteristics after adsorption between the AC and OMC sorbents suggests that the larger pore sizes in OMC facilitate diffusion of PFOA molecules into the carbon matrix and enable their adsorption, thus resulting in more significant changes to the pore texture.

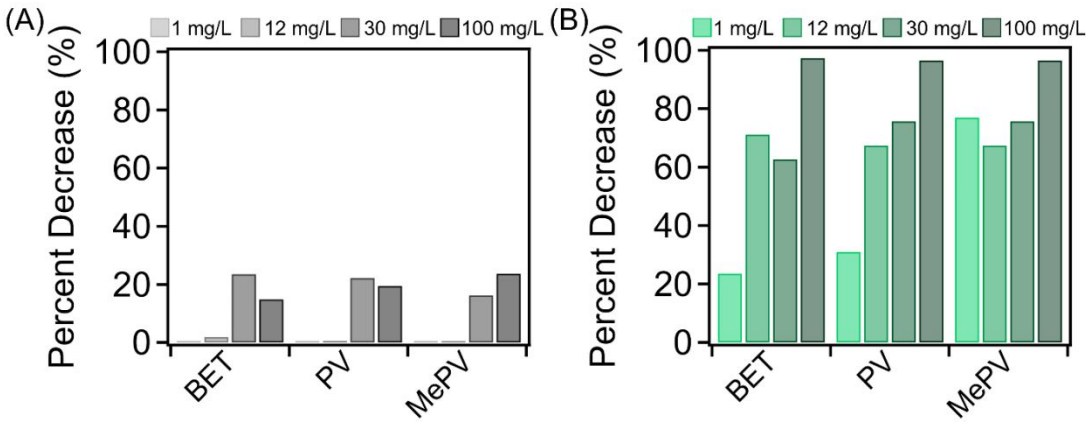

Figure 5. BET surface area (BET), total pore volume (PV), and mesopore volume (MePV) changes after adsorption of PFOA from solution concentrations of 1 mg/L, 12 mg/L, 30 mg/L, 100 mg/L for the (A) AC and (B) OMC sorbents.

Conclusion

PFAS remediation at a commercial scale relies on sorption-based processes using porous sorbents like activated carbon. In these systems, sorbent pore size plays an important role in PFAS adsorption, including controlling sorbate diffusion and sorption site accessibility. This study uses

SANS under contrast-matched conditions, combined with simulation and adsorption investigations to examine how pore size influences the morphological evolution of PFOA aggregates during adsorption, using microporous and mesoporous sorbents as models. In microporous AC sorbents, PFOA forms small structures of a few molecules, while the larger pores of OMC sorbents facilitate layered structures that extend into the pore center. Molecular dynamics simulations further reveal the progression of these layers into hemi-micelle-like assemblies at higher concentrations, emphasizing the role of mesoporosity. These findings offer critical insights into pore-size-driven PFAS aggregate formation, guiding the design of optimized sorbent materials for effective remediation.

ACKNOWLEDGMENT

M.R. would like to acknowledge funding support through the DOE SCGSR program. Z. Q. and A. G. acknowledge the support from NSF CMMI-2239408. This research used resources at the High Flux Isotope Reactor, a DOE Office of Science User Facility operated by the Oak Ridge National Laboratory. The beam time was allocated to CG2 on proposal number IPTS-31802, IPTS-30935, IPTS-31100, IPTS-28612. The authors would also like to acknowledge HPC at The University of Southern Mississippi. HPC is supported by the National Science Foundation under the Major Research Instrumentation (MRI) program via Grant # ACI 1626217.

Conflicts of interest

There are no conflicts to declare.

Author contributions

This manuscript has been prepared by contributions from all authors, who have also approved of the final version of the manuscript.

REFERENCES

[1] Lewis, R. C.; Johns, L. E.; Meeker, J. D. *Int J Environ Res Public Health*, 2015, **12**, 6098–6114.

[2] Podder, A.; Sadmani, A. H. M. A.; Reinhart, D.; Chang, N. Bin; Goel, R. *J Hazard Mater*, 2021, **419**, 126361.

[3] Yadav, S.; Ibrar, I.; Al-Juboori, R. A.; Singh, L.; Ganbat, N.; Kazwini, T.; Karbassiyazdi, E.; Samal, A. K.; Subbiah, S.; Altaee, A. *Chem Eng Res Des*, 2022, **182**, 667–700.

[4] Guo, P.; Furnary, T.; Vasiliou, V.; Yan, Q.; Nyhan, K.; Jones, D. P.; Johnson, C. H.; Liew, Z. *Environ Int*, 2022, **162**, 107159.

[5] Nguyen, T. V.; Trang, P. N.; Kumar, A. *Environ Int*, 2024, **186**, 108620.

[6] Steenland, K.; Winquist, A. *Environ Res*, 2021, **194**, 110690.

[7] Zheng, J.; Liu, S.; Yang, J.; Zheng, S.; Sun, B. *Sci Total Environ*, 2024, **953**, 176158.

[8] Glüge, J.; Scheringer, M.; Cousins, I. T.; Dewitt, J. C.; Goldenman, G.; Herzke, D.; Lohmann, R.; Ng, C. A.; Trier, X.; Wang, Z. *Environ Sci Process Impacts*, 2020, **22**, 2345–2373.

[9] Gaines, L. G. T. *Am J Ind Med*, 2023, **66**, 353–378.

[10] Cotruvo, J. A.; Goldhaber, S. B.; Cohen, A. J. B. *Groundwater*, 2023, **61**, 301–303.

[11] Li, R.; Alomari, S.; Islamoglu, T.; Farha, O. K.; Fernando, S.; Thagard, S. M.; Holsen, T. M.; Wriedt, M. *Environ Sci Technol*, 2021, **55**, 15162–15171.

[12] Buck, R. C.; Franklin, J.; Berger, U.; Conder, J. M.; Cousins, I. T.; Voogt, P. De; Jensen, A. A.; Kannan, K.; Mabury, S. A.; van Leeuwen, S. P. J. *Integr Environ Assess Manag*, 2011, **7**, 513–541.

[13] Chetverikov, S. P.; Sharipov, D. A.; Korshunova, T. Y.; Loginov, O. N. *Appl Biochem Microbiol*, 2017, **53**, 533–538.

[14] LaFond, J. A.; Hatzinger, P. B.; Guelfo, J. L.; Millerick, K.; Jackson, W. A. *Environ Sci: Adv*, 2023, **2**, 1019–1041.

[15] Wang, X.; Chen, Z.; Wang, Y.; Sun, W. *Environmental Pollution*, 2021, **291**, 118014.

[16] López-Vázquez, J.; Santos, C. S.; Montes, R.; Rodil, R.; Quintana, J. B.; Gäbler, J.; Schäfer, L.; Moreira, F. C.; Vilar, V. J. P. *Chem Eng Journ*, 2024, **482**, 148925.

[17] Mirabediny, M.; Sun, J.; Yu, T. T.; Åkermark, B.; Das, B.; Kumar, N. *Chemosphere*, 2023, **321**, 138109.

[18] Gar Alalm, M.; Boffito, D. C. *Chem Eng Journ*, 2022, **450**, 138352.

[19] Chen, C.; Ma, Q.; Liu, F.; Gao, J.; Li, X.; Sun, S.; Yao, H.; Liu, C.; Young, J.; Zhang, W. *J Hazard Mater*, 2021, **419**, 126452.

[20] Xu, B.; Ahmed, M. B.; Zhou, J. L.; Altaee, A.; Wu, M.; Xu, G. *Chemosphere*, 2017, **189**, 717–729.

[21] Banayan Esfahani, E.; Asadi Zeidabadi, F.; Zhang, S.; Mohseni, M. *Environ Sci*, 2022, **8**, 698–728.

[22] Arias Espana, V. A.; Mallavarapu, M.; Naidu, R. *Environ Technol Innov*, 2015, **4**, 168–181.

[23] Ji, W.; Xiao, L.; Ling, Y.; Ching, C.; Matsumoto, M.; Bisbey, R. P.; Helbling, D. E.; Dichtel, W. R. *J Am Chem Soc*, 2018, **140**, 12677–12681.

[24] Nguyen, T. T.; Min, X.; Xia, W.; Qiang, Z.; Khandge, R. S.; Yu, H. K.; Wang, J. W.; Wang, Y.; Ma, X. *J Memb Sci*, 2024, **705**, 122925.

[25] Wang, W.; Jia, Y.; Zhou, S.; Deng, S. *J Hazard Mater*, 2023, **460**, 132522.

[26] Zarei, A.; Khosropour, A.; Khazdooz, L.; Amirjalayer, S.; Khojastegi, A.; Zadehnazari, A.; Zhao, Y.; Abbaspourrad, A. *ACS Appl Mater Interfaces*, 2024, **16**, 9483–9494.

[27] Zhang, Y.; Kong, K.; Wu, Q.; Ma, T.; Liang, J.; Wang, R. *ChemSusChem*, 2024, **17**, e202400069.

[28] Li, R.; Alomari, S.; Stanton, R.; Wasson, M. C.; Islamoglu, T.; Farha, O. K.; Holsen, T. M.; Thagard, S. M.; Trivedi, D. J.; Wriedt, M. *Chem Mater*, 2021, **33**, 3276–3285.

[29] Li, R.; Adarsh, N. N.; Lu, H.; Wriedt, M. *Matter*, 2022, **5**, 3161–3193.

[30] FitzGerald, L. I.; Olorunyomi, J. F.; Singh, R.; Doherty, C. M. *ChemSusChem*, 2022, **15**, e202201136.

[31] Yang, Z.; Zhu, Y.; Tan, X.; Gunjal, S. J. J.; Dewapriya, P.; Wang, Y.; Xin, R.; Fu, C.; Liu, K.; Macintosh, K.; Sprague, L. G.; Leung, L.; Hopkins, T. E.; Thomas, K. V.; Guo, J.; Whittaker, A. K.; Zhang, C.; Yang, Z.; Zhu, Y.; Tan, X.; Gunjal, S. J. J.; Dewapriya, P.; Wang, Y.; Xin, R.; Fu, C.; Liu, K.; Macintosh, K.; Sprague, L. G.; Leung, L.; Hopkins, T. E.; Thomas, K. V.; Guo, J.; Whittaker, A. K.; Zhang, C. *Nat Commun*, 2024, **15**, 8269.

[32] Manning, I. M.; Chew, N. G. P.; Macdonald, H. P.; Miller, K. E.; Strynar, M. J.; Coronell, O.; Leibfarth, F. A. *Angew Chem*, 2022, **134**, e202208150.

[33] Kumarasamy, E.; Manning, I. M.; Collins, L. B.; Coronell, O.; Leibfarth, F. A. *ACS Cent Sci*, 2020, **6**, 487–492.

[34] Yang, A.; Ching, C.; Easler, M.; Helbling, D. E.; Dichtel, W. R. *ACS Mater Lett*, 2020, **2**, 1240–1245.

[35] Lin, Z. W.; Shapiro, E. F.; Barajas-Rodriguez, F. J.; Gaisin, A.; Ateia, M.; Currie, J.; Helbling, D. E.; Gwinn, R.; Packman, A. I.; Dichtel, W. R. *Environ Sci Technol*, 2023, **57**, 19624–19636.

[36] Wang, R.; Lin, Z. W.; Klemes, M. J.; Ateia, M.; Trang, B.; Wang, J.; Ching, C.; Helbling, D. E.; Dichtel, W. R. *ACS Cent Sci*, 2022, **8**, 663–669.

[37] Park, M.; Wu, S.; Lopez, I. J.; Chang, J. Y.; Karanfil, T.; Snyder, S. A. *Water Res*, 2020, **170**, 115364.

[38] Cantoni, B.; Turolla, A.; Wellmitz, J.; Ruhl, A. S.; Antonelli, M. *Sci Total Environ*, 2021, **795**, 148821.

[39] Okorie, C. J.; Ojeyemi, T.; Egbemhenghe, A.; Ali, M. Q.; Emenike, E. C.; Iwuozor, K. O.; Adeniyi, A. G. *Remediation*, 2024, **34**, e21777.

[40] Gagliano, E.; Falciglia, P. P.; Zaker, Y.; Birben, N. C.; Karanfil, T.; Roccaro, P. *Curr Opin Chem Eng*, 2023, **42**, 100955.

[41] Gagliano, E.; Sgroi, M.; Falciglia, P. P.; Vagliasindi, F. G. A.; Roccaro, P. *Water Res*, 2020, **171**, 115381.

[42] Perrich, J. R. *Activated Carbon Adsorption For Wastewater Treatment*, Taylor and Francis Group, Boca Raton, FL, 2018.

[43] Hoang, A. T.; Kumar, S.; Lichtfouse, E.; Cheng, C. K.; Varma, R. S.; Senthilkumar, N.; Phong Nguyen, P. Q.; Nguyen, X. P. *Chemosphere*, 2022, **302**, 134825.

[44] Sonmez Baghirzade, B.; Zhang, Y.; Reuther, J. F.; Saleh, N. B.; Venkatesan, A. K.; Apul, O. G. *Environ Sci Technol*, 2021, **55**, 5608–5619.

[45] Pauletto, P. S.; Bandosz, T. J. *J Hazard Mater*, 2022, **425**, 127810.

[46] Kim, G.; Mengesha, D. N.; Choi, Y. *Sep Purif Technol*, 2024, **349**, 127851.

[47] Kabiri, S.; Monaghan, C. L.; Navarro, D.; McLaughlin, M. J. *Environ Sci)*, 2024, **10**, 420–430.

[48] Maimaiti, A.; Deng, S.; Meng, P.; Wang, W.; Wang, B.; Huang, J.; Wang, Y.; Yu, G. *Chem Eng Journ*, 2018, **348**, 494–502.

[49] Karoyo, A. H.; Wilson, L. D. *J Colloid Interface Sci*, 2013, **402**, 196–203.

[50] Lei, X.; Yao, L.; Lian, Q.; Zhang, X.; Wang, T.; Holmes, W.; Ding, G.; Gang, D. D.; Zappi, M. E. *J Hazard Mater*, 2022, **421**, 126810.

[51] Meng, Y.; Gu, D.; Zhang, F.; Shi, Y.; Cheng, L.; Feng, D.; Wu, Z.; Chen, Z.; Wan, Y.; Stein, A.; Zhao, D. *Chem Mater*, 2006, **18**, 4447–4464.

[52] Qiang, Z.; Xue, J.; Cavicchi, K. A.; Vogt, B. D. *Langmuir*, 2013, **29**, 3428–3438.

[53] Wei, Y.; Hore, M. J. A. *J Appl Phys*, 2021, **129**,171101.

[54] Jeffries, C. M.; Ilavsky, J.; Martel, A.; Hinrichs, S.; Meyer, A.; Pedersen, J. S.; Sokolova, A. V.; Svergun, D. I. *Nat Rev Methods Primers*, 2021, **1**, 1–39.

[55] Heller, W. T.; Cuneo, M.; Debeer-Schmitt, L.; Do, C.; He, L.; Heroux, L.; Littrell, K.; Pingali, S. V.; Qian, S.; Stanley, C.; Urban, V. S.; Wu, B.; Bras, W. *J Appl Cryst*, 2018, **51**, 242–248.

[56] Pedersen, J. S. *Adv Colloid Interface Sci*, 1997, **70**, 171–210.

[57] Berendsen, H. J. C.; Grigera, J. R.; Straatsma, T. P. *J Phys Chem*, 1987, **91**, 6269–6271.

[58] Barbosa, G. D.; Turner, C. H. *J Mol Liq*, 2023, **389**, 122826.

[59] Malde, A. K.; Zuo, L.; Breeze, M.; Stroet, M.; Poger, D.; Nair, P. C.; Oostenbrink, C.; Mark, A. E. *J Chem Theory Comput*, 2011, **7**, 4026–4037.

[60] Thompson, A. P.; Aktulga, H. M.; Berger, R.; Bolintineanu, D. S.; Brown, W. M.; Crozier, P. S.; in 't Veld, P. J.; Kohlmeyer, A.; Moore, S. G.; Nguyen, T. D.; Shan, R.; Stevens, M. J.; Tranchida, J.; Trott, C.; Plimpton, S. J. *Comput Phys Commun*, 2022, **271**, 108171.

[61] Gowers, R. J.; Linke, M.; Barnoud, J.; Reddy, T. J. E.; Melo, M. N.; Seyler, S. L.; Domański, J.; Dotson, D. L.; Buchoux, S.; Kenney, I. M.; Beckstein, O. *scipy*, 2016, 98–105.

[62] Stukowski, A. *Model Simul Mat Sci Eng*, 2009, **18**, 015012.

[63] Dong, D.; Kancharla, S.; Hooper, J.; Tsianou, M.; Bedrov, D.; Alexandridis, P. *Phys Chem Chem Phys*, 2021, **23**, 10029–10039.

[64] Kancharla, S.; Dong, D.; Bedrov, D.; Tsianou, M.; Alexandridis, P. *Langmuir*, 2021, **37**, 5339–5347.

[65] Leung, S. C. E.; Wanninayake, D.; Chen, D.; Nguyen, N. T.; Li, Q. *Sci Total Environ*, 2023, **905**, 166764.

[66] Xu, J.; Liu, Z.; Zhao, D.; Gao, N.; Fu, X. *Sci Total Environ*, 2020, **723**, 137757.

[67] Müter, D.; Shin, T.; Demé, B.; Fratzl, P.; Paris, O.; Findenegg, G. H. *J PhysChem Lett*, 2010, **1**, 1442–1446.

[68] Wu, Y.; Ma, Y.; He, L.; Rother, G.; Shelton, W. A.; Bharti, B. *J Phys Chem C,* 2019, **123**, 9957-9966.

[69] Siefker, J.; Biehl, R.; Kruteva, M.; Feoktystov, A.; Coppens, M. O. *J Am Chem Soc*, 2018, **140**, 12720–12723.

[70] Holewinski, A.; Sakwa-Novak, M. A.; Jones, C. W. *J Am Chem Soc,* 2015, **137**, 11749-11759.

[71] Stefanopoulos, K. L.; Romanos, G. E.; Vangeli, O. C.; Mergia, K.; Kanellopoulos, N. K.; Koutsioubas, A.; Lairez, D. *Langmuir*, 2011, **27**, 7980–7985.

[72] Shin, T. G.; Müter, D.; Meissner, J.; Paris, O.; Findenegg, G. H. *Langmuir*, 2011, **27**, 5252–5263.

[73] Han, J.; Choong, C. E.; Jang, M.; Lee, J.; Hyun, S.; Lee, W. S.; Kim, M. *Chemosphere*, 2024, **365**, 143320.